

## MIT Open Access Articles

### *Operando NAP-XPS unveils differences in MoO<sub>3</sub> and Mo<sub>2</sub>C during hydrodeoxygenation*

The MIT Faculty has made this article openly available. **Please share** how this access benefits you. Your story matters.

**As Published:** 10.1038/S41929-018-0171-9

**Publisher:** Springer Science and Business Media LLC

**Persistent URL:** <https://hdl.handle.net/1721.1/135080>

**Version:** Author's final manuscript: final author's manuscript post peer review, without publisher's formatting or copy editing

**Terms of use:** Creative Commons Attribution-Noncommercial-Share Alike



# Operando NAP-XPS unveils differences in MoO<sub>3</sub> and Mo<sub>2</sub>C during hydrodeoxygenation

Karthick Murugappan<sup>1</sup>, Eric M. Anderson<sup>1</sup>, Detre Teschner<sup>2,3</sup>, Travis E. Jones<sup>2</sup>, Katarzyna Skorupska<sup>2,3</sup>, and Yuriy Román-Leshkov<sup>1\*</sup>

MoO<sub>3</sub> and Mo<sub>2</sub>C have emerged as remarkable catalysts for the selective hydrodeoxygenation (HDO) of a wide range of oxygenates at low temperatures (i.e., ≤ 673 K) and H<sub>2</sub> pressures (i.e., ≤ 1 bar). While both catalysts can selectively cleave C–O bonds, the nature of their active sites remains unclear. Here, we used operando near-ambient pressure X-ray photoelectron spectroscopy to reveal important differences in the Mo 3d oxidation states between the two catalysts during the HDO of anisole. This technique revealed that although both catalysts featured a surface oxycarbide phase, the oxygen content and the underlying phase of the material impacted the reactivity and product selectivity during HDO. MoO<sub>3</sub> transitioned between 5+ and 6+ oxidation states during operation, consistent with an oxygen vacancy driven mechanism wherein the oxygenate is activated at undercoordinated Mo sites. In contrast, Mo<sub>2</sub>C showed negligible oxidation state changes during HDO, maintaining mostly 2+ states throughout the reaction.

## Introduction

Hydrodeoxygenation (HDO) is an important upgrading strategy for converting lignocellulosic biomass to fuels and chemicals that relies on molecular H<sub>2</sub> to selectively remove oxygen in the form of water.<sup>1–13</sup> While noble metal catalysts have dominated the HDO landscape, molybdenum trioxide (MoO<sub>3</sub>)<sup>14–20</sup> and molybdenum carbide (Mo<sub>2</sub>C)<sup>21–31</sup> have recently emerged as promising earth-abundant alternatives that can selectively cleave C–O bonds under mild conditions. In contrast to state-of-the-art noble metal catalysts, MoO<sub>3</sub> and Mo<sub>2</sub>C catalysts produce unsaturated hydrocarbons, while concurrently minimizing both the saturation of C=C double bonds and the cleavage of C–C bonds.

Román-Leshkov *et al.* showed that MoO<sub>3</sub> converts a wide-range of linear and aromatic oxygenates into olefinic and aromatic hydrocarbons, respectively, with high selectivities (>97%) using low H<sub>2</sub> pressures (≤ 1 bar) and temperatures below 673 K.<sup>14</sup> Post-reaction characterization studies revealed that MoO<sub>3</sub> underwent partial carburization to form an oxycarbohydride (MoO<sub>x</sub>C<sub>y</sub>H<sub>z</sub>) featuring a large proportion of Mo<sup>5+</sup> surface species.<sup>15</sup> It was hypothesized that these undercoordinated species (i.e. oxygen vacancies) were responsible for activating the C–O bond and that the lattice carbon in MoO<sub>x</sub>C<sub>y</sub>H<sub>z</sub> played a crucial role in preventing the over-reduction of Mo<sup>5+</sup> into less active Mo<sup>4+</sup> sites.<sup>15</sup>

In parallel, Bhan and co-workers showed that Mo<sub>2</sub>C is highly selective for cleaving strong phenolic C–O bonds at atmospheric H<sub>2</sub> pressures and temperatures ranging from

420 to 553 K.<sup>22, 23, 26, 28, 29</sup> For instance, Mo<sub>2</sub>C converted anisole to benzene with selectivity values >90% at 423 K. Detailed kinetic studies revealed that two distinct sites are required: one for H<sub>2</sub> dissociative adsorption and one for oxygenate activation.<sup>22, 26, 29</sup> The site required for oxygenate adsorption was hypothesized to be metal-like in nature based on the invariant product generation rates when normalized by *ex situ* CO chemisorption.<sup>22, 26</sup> In a subsequent study, an oxygen mass balance performed during transient HDO experiments revealed oxygen incorporation equivalent to ~0.29 monolayers.<sup>27</sup> Given the lack of bulk structural changes, this oxidation was hypothesized to be a surface and/or a subsurface phenomenon.<sup>26–29</sup>

Notwithstanding this evidence, the exact nature of the active sites in both materials remains unresolved. On the one hand, the presence of oxycarbide sites may suggest a common HDO pathway for both materials. Indeed, although CO chemisorption is typically used to titrate metallic sites that may be present in Mo<sub>2</sub>C and not in MoO<sub>3</sub>, CO can also bind to the undercoordinated sites of MoO<sub>x</sub>C<sub>y</sub>H<sub>z</sub>.<sup>27</sup> Hence, the potential active site for oxygenate adsorption in Mo<sub>2</sub>C could be either metallic or an oxygen vacancy similar to that observed over MoO<sub>3</sub>. On the other hand, reactivity data has shown different HDO product distributions for both materials when compared at identical conditions (Supplementary Fig. 1), thus suggesting different site speciation over the catalytic surfaces.

Unfortunately, *ex situ* characterization techniques do not allow us to establish clear structure-performance relationships for these materials. Although post-reaction

<sup>1</sup>Department of Chemical Engineering, Massachusetts Institute of Technology, Cambridge, Massachusetts 02139, United States. <sup>2</sup>Fritz-Haber-Institut der Max-Planck-Gesellschaft, Abteilung Anorganische Chemie, Berlin 14195, Germany. <sup>3</sup>Max-Planck-Institut für Chemische Energiekonversion, Stiftstr. 34–36, 45470 Mülheim a. d. Ruhr, Germany. \*e-mail: yroman@mit.edu

X-ray photoelectron spectroscopy (XPS) of spent  $\text{MoO}_3$  provided insights into the nature of the catalysts after reaction, this *ex situ* approach does not capture the dynamics of the catalyst surface under the reaction conditions.<sup>32</sup> More importantly,  $\text{Mo}_2\text{C}$  is highly oxophilic, and readily forms an oxide passivation layer when exposed to  $\text{O}_2$ .<sup>33-35</sup> This changes the surface structure from that present during reaction and convolutes data from *ex situ* characterization methods.<sup>34</sup> Since both catalysts undergo significant structural and surface modifications during the course of the reaction, an *in situ* surface characterization technique is required to interrogate the active sites responsible for HDO.

Here, we used operando near-ambient pressure XPS (NAP-XPS) to probe the nature of active sites over  $\text{MoO}_3$  and  $\text{Mo}_2\text{C}$  catalysts during HDO of anisole at 593 K and  $\text{H}_2$  pressures ( $\leq 1$  mbar). Using synchrotron radiation, we were able to increase surface sensitivity by modulating the incident photon energies to measure ejected photoelectrons at lower kinetic energies than those that measured with traditional ultra-high vacuum (UHV) XPS.<sup>32</sup> Our study revealed that both catalysts predominantly produced benzene as the major product under the reaction conditions investigated. However, the changes in Mo 3d oxidation states during HDO were drastically different across both materials. The Mo 3d core level spectra were rigorously analysed with the aid of density functional theory (DFT) calculations to identify the various contributions associated with different chemical environments. In addition to Mo 3d spectra, O 1s, C 1s, surface elemental composition, C-Mo and O-Mo ratios were examined to gain insight into the cause of deactivation. Thus, our work provides a robust framework for interpreting Mo 3d XPS data for  $\text{MoO}_3$  and  $\text{Mo}_2\text{C}$  catalysts.

## Results

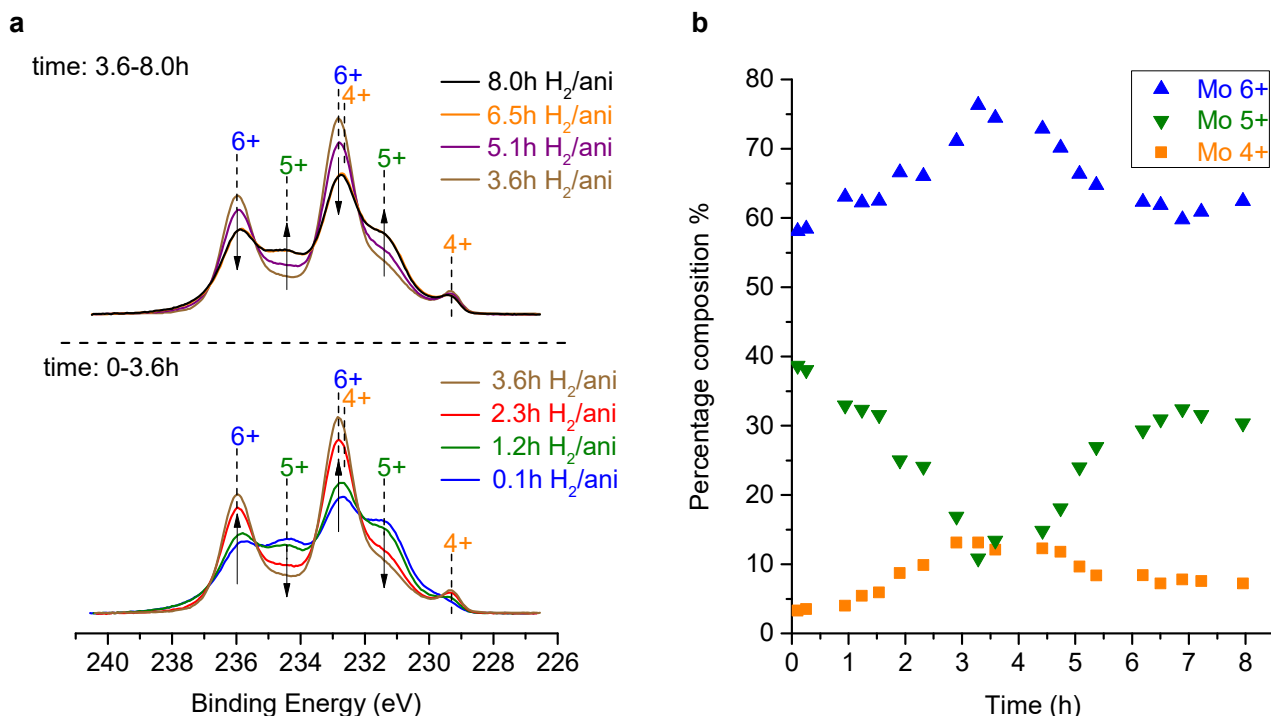
**NAP-XPS measurements.** In order to investigate the nature of the active sites during HDO, NAP-XPS measurements were performed over both  $\text{MoO}_3$  and  $\text{Mo}_2\text{C}$  samples under identical reaction conditions ( $P_{\text{total}} = 1$  mbar with  $P_{\text{anisole}} = 0.005$  mbar and balance  $\text{H}_2$  at 593 K). Due to the lack of reliable fitting strategies for surface-sensitive Mo 3d spectra for  $\text{Mo}_2\text{C}$ , DFT calculations were used to aid in developing a robust fit parameter set. In short, we benchmarked our theoretical approach first by simulating known Mo 3d line shapes of metallic Mo and  $\text{MoO}_2$ , followed by calculating the line shape of  $\text{Mo}_2\text{C}$  (see Supplementary Methods I, Supplementary Fig. 2 and Supplementary Table 1).

Figure 1a shows the Mo 3d XPS spectra acquired over pre-reduced  $\text{MoO}_3$  during reaction. Detailed information about Mo 3d binding energies, deconvolution parameters and a sample deconvoluted spectrum are available in the Supplementary Information (Supplementary Methods II, Supplementary Tables 1-3, and Supplementary Fig. 3). In the first 3.6 h, there is a clear continuous oxidation of  $\text{Mo}^{5+}$  to  $\text{Mo}^{6+}$ , as seen by the lower intensities of  $\text{Mo}^{5+}$  peaks and the sharper  $\text{Mo}^{6+}$  peaks. Interestingly, after *ca.* 4 h on stream, the proportion of  $\text{Mo}^{6+}$  started to decline with a concomitant increase of  $\text{Mo}^{5+}$ , ultimately reaching a steady state. No peaks correspond-

ing to  $\text{Mo}^{2+}$  ( $\text{Mo}_2\text{C}$ ) or Mo (Mo metal) were observed. The distribution of Mo oxidation states was tracked as a function of time as seen in Figure 1b. Specifically, the proportion of Mo oxidation states changed from 39%  $\text{Mo}^{5+}$  and 58%  $\text{Mo}^{6+}$  to 11%  $\text{Mo}^{5+}$  and 76%  $\text{Mo}^{6+}$  in the first 3.3 h, before reaching a steady state distribution of 31%  $\text{Mo}^{5+}$  and 61%  $\text{Mo}^{6+}$ . Similarly,  $\text{Mo}^{4+}$  mirrored the trends observed with  $\text{Mo}^{6+}$  increasing from ~3% to 13% in the first 3.3 h, before decreasing to a steady state composition of ~8%  $\text{Mo}^{4+}$  species. A repeat of the experiment with a new  $\text{MoO}_3$  pellet resulted in similar trends (Supplementary Figs. 6-8).

Control experiments on fresh  $\text{MoO}_3$  samples were used to gain insights into the observed changes in Mo oxidation states during HDO. First, the Mo 3d spectra of untreated  $\text{MoO}_3$  (i.e. not pretreated with  $\text{H}_2$ ) acquired at 593 K in 1 mbar  $\text{N}_2$  flow predominantly featured a combination of  $\text{Mo}^{6+}$  and  $\text{Mo}^{5+}$  states with their respective  $3d_{5/2}$  peaks located at 232.8 eV<sup>36</sup> and 231.5 eV<sup>36-38</sup> (Supplementary Fig. 9). The presence of  $\text{Mo}^{5+}$  species indicates that the sample underwent partial thermal reduction. Bulk  $\text{MoO}_2$  (Supplementary Fig. 10) featured oxidation states corresponding to  $\text{Mo}^{4+}$  (52%), with additional contributions of  $\text{Mo}^{5+}$  (23%) and  $\text{Mo}^{6+}$  states (25%). Although most reports typically model  $\text{Mo}^{4+}$  as one set of doublet peaks,<sup>38, 39</sup> recent surface science literature has shown that  $\text{Mo}^{4+}$  actually consists of 2 pairs of doublets with one narrow, asymmetric pair associated with a screened metallic environment, and one broader, more symmetric pair corresponding to an unscreened environment.<sup>40-42</sup> Here, we also associated the  $\text{Mo}^{4+}$  state to 2 sets of doublets with their Mo  $3d_{5/2}$  peaks located at *ca.* 229.3 and 230.6 eV. Next, a pre-reduced  $\text{MoO}_3$  sample exposed to only  $\text{H}_2$  gas (i.e. in the absence of anisole) at 593 K showed a decreasing proportion of  $\text{Mo}^{6+}$  species from *ca.* 67% to 61% with a concomitant increase in  $\text{Mo}^{5+}$  from *ca.* 32% to 38% in the first 2.2 h, before approaching a steady state distribution of *ca.* 36%  $\text{Mo}^{5+}$  and 62%  $\text{Mo}^{6+}$  thereafter (Supplementary Figs. 11, 12).

The HDO of anisole was investigated over  $\text{Mo}_2\text{C}$  after it was treated for 3 h with  $\text{H}_2$  at 593 K (Supplementary Fig. 13). This pre-reduction was necessary to remove any surface oxides formed during sample handling and loading pre-reaction (*vide infra*). In stark contrast to the Mo 3d spectra of pre-reduced  $\text{MoO}_3$ , no significant changes were observed in the Mo oxidation states over  $\text{Mo}_2\text{C}$  during the course of the HDO reaction (see Fig. 2a). The distribution of Mo species remained relatively constant at *ca.* 84%  $\text{Mo}^{2+}$ , 14%  $\text{Mo}^{4+}$ , 1%  $\text{Mo}^{5+}$  and 1%  $\text{Mo}^{6+}$  (see Fig. 2b) throughout the reaction (~7 h), and resembled that obtained after the  $\text{H}_2$  reduction. A repeat experiment with a new  $\text{Mo}_2\text{C}$  pellet showed similar trends (Supplementary Figs. 14-17). A control experiment with fresh  $\text{Mo}_2\text{C}$  in the presence of just  $\text{H}_2$  (i.e., in the absence of anisole) was performed prior to the HDO experiment to determine the Mo 3d binding energies corresponding to  $\text{Mo}_2\text{C}$ . The corresponding Mo 3d binding energies, deconvolution fit parameters and a representative deconvoluted spectrum for  $\text{Mo}_2\text{C}$  are shown in the Supplementary Information (Supplementary Methods II, Supplementary Tables 1, 4-5 and Supplementary Fig. 4). Although most reports associate  $\text{Mo}^{2+}$  in  $\text{Mo}_2\text{C}$  with a single set of



**Fig. 1** | NAP-XPS of pre-reduced MoO<sub>3</sub> during HDO of anisole at photon energy of 473 eV. **a**, Normalized Mo 3d spectra at few selected time points from the entire data set for better visualization **b**, Percent composition of Mo oxidation states with time. Reaction conditions: T = 593 K, P<sub>total</sub> = 1 mbar (P<sub>anisole</sub> = 0.005 mbar, balance H<sub>2</sub>).

doublet, our theoretical analysis (Supplementary Fig. 2) showed that Mo<sup>2+</sup> features three sets of doublets. The dominant doublet corresponding to Mo<sup>2+</sup> is strongly asymmetric in nature and corresponds to the Mo 3d<sub>5/2</sub> signal at 228.2 eV (Supplementary Fig. 18a), in agreement with prior literature reports.<sup>43, 44</sup> In addition, two minor doublets with their Mo 3d<sub>5/2</sub> bands centred at ca. 228.9

and 231.9 eV also correspond to Mo<sup>2+</sup> (Supplementary Fig. 4). Despite our attempts to minimize air exposure, a ca. 0.33 nm thick oxide overlayer (see Supplementary Methods III, Supplementary Table 6) exists on the 'fresh' Mo<sub>2</sub>C surface as evidenced by the presence of a broad shoulder in the Mo 3d spectra at higher binding energies. Peak deconvolution revealed that ca. 72% of Mo species exist as

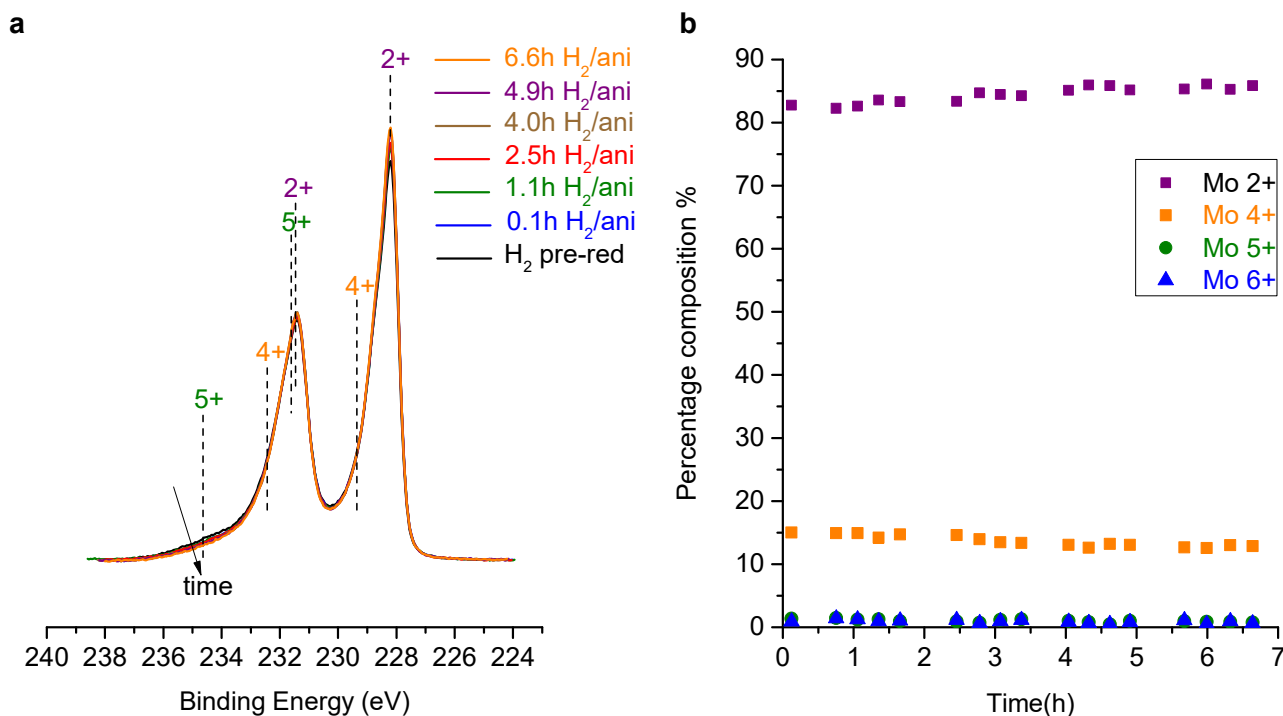


**Fig. 2** | NAP-XPS of Mo<sub>2</sub>C during HDO of anisole at photon energy of 473 eV. **a**, Normalized Mo 3d spectra at few selected time points from the entire data set for better visualization **b**, Percent composition of Mo oxidation states with time. Reaction conditions: T = 593 K, P<sub>total</sub> = 1 mbar (P<sub>anisole</sub> = 0.005 mbar, balance H<sub>2</sub>) and H<sub>2</sub> pre-reduction = 3 h.

Mo<sup>2+</sup>, associated with carbidic Mo<sub>2</sub>C, while Mo<sup>4+</sup>, Mo<sup>5+</sup> and Mo<sup>6+</sup> constitute the remaining 15%, 10% and 3% respectively, associated with oxidic species. We note that a conservative Mo<sub>2</sub>C fitting was performed wherein the asymmetry parameter of the dominant Mo<sup>2+</sup> peak was not allowed to be too high to obtain reasonable fits, thus potentially underestimating the Mo<sup>2+</sup> and overestimating the higher oxide contributions. The presence of residual oxygen on freshly synthesized Mo<sub>2</sub>C was also observed by Bhan and co-workers.<sup>29</sup> The intense carbidic C 1s signal at ca. 283.1 eV<sup>45-47</sup> is a strong indication that the surface is carbidic or oxycarbidic in nature (Supplementary Fig. 18b). In addition, a signal at 284.5 eV associated with graphitic carbon,<sup>43</sup> and peaks at 285.9 and 288.1 eV corresponding to oxidized carbon entities (C–O<sup>48</sup> and C=O respectively) are also visible in the spectrum. As seen from Supplementary Fig. 19, maintaining the catalyst under H<sub>2</sub> flow at 593 K decreased the oxide layer on the surface, but did not completely eliminate it. Specifically, the amount of Mo<sup>2+</sup> increased by ca. 10% after 3 h under H<sub>2</sub> flow, and appeared to remain relatively constant at this value thereafter. As such, a 3 h pre-reduction was performed before the HDO reaction. The invariance in amount of Mo<sup>2+</sup> after 3 h suggests that the remaining oxide layer (corresponding to Mo<sup>4+</sup>, Mo<sup>5+</sup> and Mo<sup>6+</sup> species) on the carbide is likely more difficult to be removed under these mild reduction conditions, consistent with prior reports wherein temperatures above 823 K was required to remove residual oxygen from fresh Mo<sub>2</sub>C catalysts.<sup>29</sup>

**Micro-GC results.** Benzene was the major HDO product observed over both MoO<sub>3</sub> (Supplementary Fig. 20) and Mo<sub>2</sub>C (Supplementary Fig. 21). However, the rates of benzene formation were very different. Upon introduction of the H<sub>2</sub>-anisole saturated stream over pre-reduced MoO<sub>3</sub>, the benzene concentration increased sharply to reach a maximum in ca. 1.3 h, before very slowly decreasing over the next 6.7 h (Supplementary Fig. 20). In contrast, the benzene concentration reached a maximum in just ca. 0.4 h over Mo<sub>2</sub>C, before dropping rapidly in the next 2.5 h (Supplementary Fig. 21). Benzene content continued to decrease thereafter, albeit at a slower rate. The presence of two deactivation profiles over Mo<sub>2</sub>C is also consistent with observations from anisole HDO experiments performed at 593 K and atmospheric H<sub>2</sub> pressures over bulk and supported Mo<sub>2</sub>C (Supplementary Figs. 22, 23). Notably, Mo<sub>2</sub>C generated almost an order of magnitude more benzene than MoO<sub>3</sub>, thereby suggesting that although both catalysts produced benzene, Mo<sub>2</sub>C was significantly more active than MoO<sub>3</sub> under similar reaction conditions. We note that while Mo<sub>2</sub>C (~25 m<sup>2</sup>/g) has a higher BET surface area than MoO<sub>3</sub> (~5 m<sup>2</sup>/g) before reaction, Delporte *et al.* showed that the surface area of MoO<sub>3</sub> increased from 4 m<sup>2</sup>/g to 150 m<sup>2</sup>/g over 15 hours in the presence of either H<sub>2</sub> or H<sub>2</sub>/hydrocarbon mixture at 623 K.<sup>49</sup> Our catalyst likely undergoes a similar increase in surface in the presence of H<sub>2</sub>/anisole mixture, although the extent of such increase is uncertain because the total pressure employed was significantly lower (1 mbar). Normalizing the rate by the pre-reaction surface area (i.e., a higher bound for MoO<sub>3</sub>) still indicated that Mo<sub>2</sub>C is a more active HDO catalyst than MoO<sub>3</sub>. Minor products typically observed

during anisole HDO at 593 K and 1.013 bar of H<sub>2</sub> over MoO<sub>3</sub>, such as phenol, cresols, toluene and methane, were not observed during NAP-XPS experiments (P<sub>H<sub>2</sub></sub> < 0.001 bar).<sup>15</sup> Since the H<sub>2</sub> pressure employed in this study is 3 orders of magnitude lower than that used under typical reactivity studies, the generation of these minor products probably falls under the detection limit of the micro-GC detector. As expected, benzene was the dominant product over Mo<sub>2</sub>C, consistent with the high benzene selectivity (≥94% selectivity on C<sub>6</sub><sup>+</sup> basis) observed during anisole HDO at 593 K, 1 bar H<sub>2</sub> pressure. This value is slightly higher than that observed by Bhan and co-workers during anisole HDO at 150°C<sup>26, 27</sup> and this difference can be attributed to the absence of cyclohexane formed from the sequential hydrogenation of benzene at 593 K. Thermodynamic calculations show that benzene hydrogenation to cyclohexane is unfavourable (ΔG<sub>reaction</sub> = +16.69 kJ/Mol) at 593 K (see Supplementary Table 11).<sup>50, 51</sup> However, since no cyclohexane was detected, the calculated approach to equilibrium (see Supplementary Table 11) was likely much smaller than 1, thus indicating that benzene hydrogenation was not thermodynamically limited but likely kinetically controlled.<sup>26, 51</sup> This low hydrogenation rate suggests suppressed hydrogenation activity of the oxygen-modified Mo<sub>2</sub>C catalyst, as previously observed in the presence of oxygenated reactants such as anisole and other lignin-derived aromatics.<sup>26, 28</sup> Direct HDO of anisole over Mo<sub>2</sub>C typically yields benzene and methanol, with the latter undergoing further HDO to form methane and water.<sup>26</sup> However, no peaks corresponding to methane or methanol were observed in this study, likely due to the low amounts produced that approached the detection limit of the micro-GC (10 ppm).

**Powder X-ray Diffraction (PXRD).** PXRD patterns of pre-reduced MoO<sub>3</sub> showed that the bulk MoO<sub>3</sub> structure was preserved during the 3 h H<sub>2</sub> pretreatment (Supplementary Fig. 24). Similarly, the PXRD pattern of fresh Mo<sub>2</sub>C showed only peaks associated with β-Mo<sub>2</sub>C, with no visible diffractions from MoO<sub>2</sub> (see Supplementary Fig. 25). PXRD patterns of spent MoO<sub>3</sub> catalysts did not show any appreciable changes in the bulk MoO<sub>3</sub> structure (Supplementary Fig. 26). No new peaks corresponding to the MoO<sub>x</sub>C<sub>y</sub>H<sub>z</sub> or MoO<sub>2</sub> were observed, contrasting to the PXRD patterns observed after HDO of m-cresol at 593 K.<sup>15</sup> This can be attributed to the significantly lower H<sub>2</sub> pressure employed here which might not be high enough to cause a bulk transformation of the catalyst. While bulk oxycarbide was not observed after reaction, the increased presence of Mo<sup>5+</sup> observed at the surface is indicative of surface oxycarbide formation (*vide infra*), consistent with our previous studies.<sup>15</sup> Similarly, PXRD patterns of spent Mo<sub>2</sub>C catalysts (Supplementary Fig. 27) reveal that the bulk structure of Mo<sub>2</sub>C was preserved during HDO reaction, in agreement with prior observations by Bhan.<sup>26</sup>

## Discussion

Mo 3d spectra acquired during HDO of anisole over pre-reduced MoO<sub>3</sub> across both replicate experiments featured an initial oxidation phase (~4 h) followed by a reduction phase, before approaching a steady state composition. Effectively, the catalyst underwent an initial transient

oxidation-reduction cycle to move closer to its working state, as seen by the relatively constant distribution of Mo species towards the end of the experiment. During the initial stages of the reaction, the anisole feed oxidized the Mo<sup>5+</sup> surface species to Mo<sup>6+</sup> species, even at the high H<sub>2</sub>-anisole molar ratios (~215) used. Similarly, the proportion of Mo<sup>4+</sup> first increased, thus implying that some Mo sites were over-reduced to Mo<sup>4+</sup> during the pre-reduction, before reaching a steady value of ca. 8%. This smaller proportion of Mo<sup>4+</sup> on the surface compared to the Mo<sup>5+</sup> or Mo<sup>6+</sup> states indicates that Mo<sup>4+</sup> does not play a significant role in HDO. We note that the amount of Mo<sup>4+</sup> observed during these experiments was significantly lower than that observed in our prior work (49% Mo<sup>4+</sup>),<sup>16</sup> likely due to the slower rate of reduction at the lower H<sub>2</sub> pressures used in the NAP-XPS chamber. We also note that no oxidation was observed in control experiments with MoO<sub>3</sub> in the absence of feed (anisole), thereby ruling out any significant oxygen contamination in the chamber. Since the oxidation was only observed upon introduction of feed, it is likely a direct effect from the interaction of the oxygenate with the catalyst surface. Once the feed is introduced, oxygen from the anisole can bind favourably to the undercoordinated Mo sites (Mo<sup>5+</sup>), thereby oxidizing the Mo species. This result is in line with observations by Delporte *et al.* wherein carbon atoms from the reactant rapidly fill oxygen vacancies to form an oxycarbohydride phase, thereby preventing the formation of MoO<sub>2</sub>.<sup>49</sup> Similarly, our previous work also revealed that pre-reduced MoO<sub>3</sub> transformed into a mixture of MoO<sub>x</sub>C<sub>y</sub>H<sub>z</sub> and MoO<sub>2</sub> after coming into contact with m-cresol for 0.5 h.<sup>15</sup> In this study, oxidation continued up to ~ 4 h, at which point the catalyst transitioned to its working state with an equilibrated ratio of Mo<sup>6+</sup>/Mo<sup>5+</sup> and steady state HDO rates. This oxidation-reduction cycle could possibly depict the actual turnovers observed on the MoO<sub>3</sub> catalytic surface. Taken together, the interplay of Mo<sup>5+</sup> and Mo<sup>6+</sup> states is strong evidence that Mo<sup>5+</sup> is active for HDO under these reaction conditions. Furthermore, Mo 3d spectra acquired at higher photon energies of 946 eV and 1486.7 eV (see Supplementary Figs. 28-30) revealed that the surface of MoO<sub>3</sub> featured more Mo<sup>5+</sup> and less Mo<sup>6+</sup> states than the bulk, thus further confirming that Mo<sup>5+</sup> is the active site responsible for HDO over MoO<sub>3</sub>. Adsorption of oxygenates onto such undercoordinated Mo sites is also consistent with mechanisms proposed during HDO of acrolein<sup>52</sup> and acetaldehyde<sup>53</sup> over MoO<sub>3</sub>. Similarly, the same depth profile analysis (Supplementary Figs. 29,30) showed that the bulk was more enriched with Mo<sup>4+</sup> states than the surface and that the amount of Mo<sup>4+</sup> in bulk increased during reaction, indicating bulk-like over-reduction i.e. transport of oxygen vacancies propagating down to the bulk. This observation is also consistent with the rapid deactivation observed over MoO<sub>3</sub> at 673 K during HDO of m-cresol, attributed to the complete bulk-reduction of MoO<sub>3</sub> to MoO<sub>2</sub> (Mo<sup>4+</sup>),<sup>15</sup> indicating that Mo<sup>4+</sup> is not that active for HDO.

Analysis of the Mo 3d spectra of Mo<sub>2</sub>C revealed that the dominant Mo<sup>2+</sup> phase was maintained throughout the reaction, showing negligible oxidation even in the presence of the oxygenate feed. We note that the H<sub>2</sub> pre-reduction, as expected, led to an initial increase in the Mo<sup>2+</sup> content (from 72% to 83%) and a corresponding

decrease in the oxide overlayer thickness (0.33 nm to 0.20 nm, see Supplementary Table 6). However, both the composition of Mo oxidation states and the oxygen coverage did not vary significantly during the HDO reaction, similar to that reported by Schaidle *et al.* during HDO of acetic acid over Mo<sub>2</sub>C.<sup>54</sup> The prevalence of Mo<sup>2+</sup> species and the negligible changes in Mo<sup>5+</sup>/Mo<sup>6+</sup> oxidation states imply that the dominant carbide/oxycarbide phase is likely responsible for HDO over Mo<sub>2</sub>C. This presence of oxycarbide phase during HDO was also illustrated by Schaidle *et al.* using DFT calculations, wherein a submonolayer of oxygen was shown to exist on the Mo-Mo<sub>2</sub>C(001) and C-Mo<sub>2</sub>C(001) surfaces during HDO of acetic acid.<sup>54</sup> Using a combination of *in situ* diffuse reflectance infrared Fourier transform spectroscopy (DRIFTS), temperature-programmed desorption of ammonia (NH<sub>3</sub>-TPD) and DFT calculations, a 0.50 monolayer O/C-Mo<sub>2</sub>C(001) was proposed to be the likely active catalyst surface under the reaction conditions investigated in their study.<sup>54</sup>

Based on Mo<sub>2</sub>C's nearly invariant Mo 3d spectra, *in situ* oxidation probably cannot account for the observed catalyst deactivation. Bhan and co-workers attributed catalyst deactivation both to mild coke formation and *in situ* oxidation.<sup>27</sup> If *in situ* oxidation were a major cause of deactivation, the proportion of higher Mo oxidation states (i.e. Mo<sup>4+</sup>, Mo<sup>5+</sup> and Mo<sup>6+</sup>) would have increased with a concurrent decrease in the presence of Mo<sup>2+</sup> species. Furthermore, XPS of spent supported Mo<sub>2</sub>C catalysts (performed using an air-free transfer vessel with UHV XPS) after HDO of anisole at 593 K, 1 bar H<sub>2</sub> also revealed that the dominant Mo<sup>2+</sup> state was maintained during the reaction even after 24 h with no appreciable surface oxidation (Supplementary Fig. 31), thereby excluding *in situ* oxidation as a cause for the observed deactivation even for atmospheric H<sub>2</sub> experiments. However, the O 1s spectra featured a signal at ca. 532.7 eV (Supplementary Figs. 32, 33) that can be attributed to the oxygen present in anisole-derived reaction intermediates or to methoxy species on the catalyst surface.<sup>26, 55</sup> The signal increased during the reaction, implying growing oxygenate adsorption and potentially leading to deactivation by blocking some of the sites. Although this increase is also consistent with the oxygen incorporation reported by Bhan,<sup>27</sup> it seems to be a minor effect since it did not change the relative ratio of Mo oxidation states or the O/Mo ratios (Supplementary Figs. 34, 35) as reported in Schaidle's study.<sup>54</sup> It is possible that the rates of oxygen incorporation and surface reduction could have reached equilibrium, thereby leading to minimal changes on the quantity of O on the surface measured by XPS. This result is in agreement with prior reports wherein *in situ* oxidation predominantly occurred during the transient phase of HDO and that no further oxygen incorporation was observed during steady state HDO.<sup>27</sup> Similarly, since 'fresh' Mo<sub>2</sub>C already had some oxygen on the surface prior to reaction (ca. 0.20 nm oxide overlayer), only minute amounts of oxygen were likely incorporated during the reaction. Hence, although *in situ* oxidation cannot be excluded as a cause for deactivation observed in this study, it likely plays only a minor role in the overall decrease in catalyst performance.

The role of coking in catalyst deactivation was investigated by analysing the C 1s spectra, the surface ele-

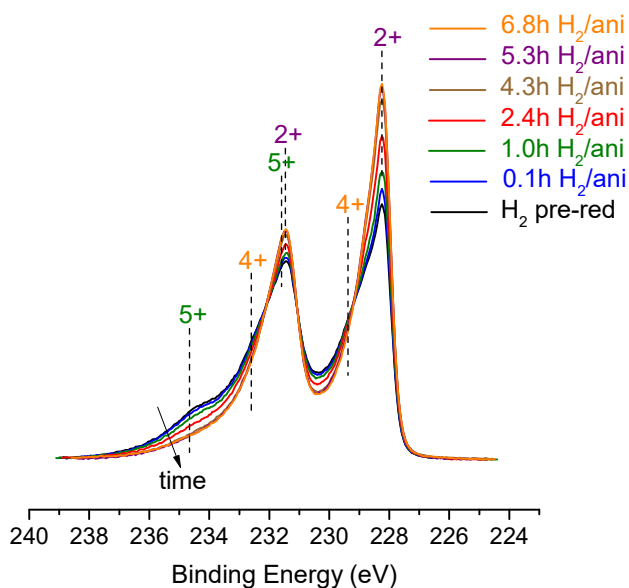


**Fig. 3 | Normalized Mo 3d spectra of passivated Mo<sub>2</sub>C (Mo<sub>2</sub>C-pass) during HDO of anisole measured at photon energy of 473 eV.** Reaction conditions: T = 593 K, P<sub>total</sub> = 1 mbar (P<sub>anisole</sub> = 0.005 mbar, balance H<sub>2</sub>) and H<sub>2</sub> pre-reduction = 3 h

mental composition and the C/Mo atomic ratios. The time-resolved C 1s spectra and the composition of different C 1s components showed no significant changes (Supplementary Figs. 37-39), suggesting that the nature of the surface carbon species was largely invariant throughout the reaction. However, surface elemental quantification (Supplementary Methods IV) revealed that C content increased by ~6% (Supplementary Fig. 40). Similarly, the atomic C/Mo ratio as measured by XPS (Supplementary Fig. 41) increased by ca. 14%, indicating a growing amount of carbonaceous deposits on the surface during the course of reaction. The rise in both surface concentration of atomic carbon and C-Mo ratios across duplicate experiments (Supplementary Figs. 42-44) is in agreement with the observations by Bhan *et al.*<sup>27</sup> and Schaidle *et al.*<sup>54</sup> Taken together, these data are strong evidence that coking is likely the major cause of deactivation route for Mo<sub>2</sub>C under the reaction conditions investigated here.

In order to understand the effect of an oxygen overlayer on the carbide surface on the HDO reactivity, a passivated carbide (Mo<sub>2</sub>C-pass) was investigated under identical reaction conditions. The passivation oxide overlayer on Mo<sub>2</sub>C-pass was determined to be approximately 1.34 nm, roughly 4 times thicker than that observed over fresh Mo<sub>2</sub>C. High Mo oxidation states dominated the Mo 3d spectra of Mo<sub>2</sub>C-pass (Supplementary Fig. 45), with only a small contribution from Mo<sup>2+</sup> (20% of the Mo surface species), which is significantly lower than that for fresh Mo<sub>2</sub>C (72%). The C 1s spectrum shows a carbidic signal at 283.2 eV, albeit less intense than that observed with fresh Mo<sub>2</sub>C (Supplementary Fig. 46). The signals at 285.9 and 288.1 eV, associated with oxidized carbon are stronger than those of fresh Mo<sub>2</sub>C. Supplementary Figure 47 shows that the passivated layer gets partially reduced during the H<sub>2</sub> treatment, as seen by an increase in the fraction of Mo<sup>2+</sup> from 20% to 55% and a corresponding

decrease in oxygen coverage to a ca. 0.57 nm oxide overlayer or roughly 1.8 monolayers (based on a Mo-O bond distance of 0.318 nm<sup>56</sup>), similar to the 1.3 monolayers observed by Bhan on a passivated Mo<sub>2</sub>C catalyst after H<sub>2</sub> treatment.<sup>27</sup>

The anisole feed did not further oxidize the Mo species on Mo<sub>2</sub>C-pass (see Fig. 3). In fact, the oxide layer continued to decrease in intensity during the reaction. Supplementary Figure 48 shows that the combined proportion of Mo<sup>4+</sup>, Mo<sup>5+</sup> and Mo<sup>6+</sup> decreased from ca. 45% to 27% during reaction in the first 4 h, while the amount of Mo<sup>2+</sup> concurrently increased from ca. 55% to 73%. The composition of Mo species was relatively constant after this 4 h time period, analogous to the trend observed with fresh Mo<sub>2</sub>C. Similarly, the oxygen coverage further decreased to 0.27 nm oxide overlayer, approaching the oxygen coverage values observed over fresh Mo<sub>2</sub>C after HDO reaction. Interestingly, although Mo<sub>2</sub>C-pass sample showed similar amounts of reactivity towards benzene production (Supplementary Fig. 49) compared to fresh Mo<sub>2</sub>C, this material also generated small quantities of toluene. This alkylation product is typically observed on bulk MoO<sub>3</sub><sup>14, 15</sup> and is also a minor alkylation product observed on H<sub>2</sub>-activated passivated Mo<sub>2</sub>C during HDO of anisole.<sup>26</sup> The presence of toluene indicates that the surface of the passivated Mo<sub>2</sub>C features Brønsted acidity,<sup>51</sup> consistent with previous reports.<sup>54, 57</sup> The presence of acid sites on Mo<sub>2</sub>C is dependent on many factors such as carburization conditions, passivation treatment, oxygen removal efficiency during H<sub>2</sub> pre-reduction, and the presence of oxygen co-feed or any other oxygenates during reaction. Sullivan *et al.* used 2,6-di-tert-butylpyridine titrations to reveal that Brønsted acid sites were responsible for the dehydration of isopropanol (IPA) to propylene over an oxygen-modified Mo<sub>2</sub>C and that these acid site densities can be reversibly tuned by a factor of ~ 30 using an O<sub>2</sub> co-feed.<sup>58</sup> Furthermore, Badour *et al.* showed that the proportion of acid sites can be tuned by the phase/composition of Mo<sub>2</sub>C while the acid strength itself can be varied by the carbide particle size.<sup>59</sup> In summary, acid sites can be either found inherently on Mo<sub>2</sub>C or can be formed either during pre-treatment or during reaction. However, the significance of these acid sites with respect to controlling reactivity is reaction-dependent. In the reaction investigated in our study, since anisole does not have a sp<sup>3</sup>-hybridized β-hydrogen, it cannot undergo dehydration, thus leading to deoxygenation mechanisms different from those observed during dehydration in the above-mentioned studies. The O 1s and C 1s spectra, as well as the elemental surface composition of carbon and atomic C-Mo ratios also showed similar trends to those observed with fresh Mo<sub>2</sub>C (Supplementary Figs. 50-53). Mo<sub>2</sub>C-pass featured a single deactivation regime (Supplementary Fig. 49), in comparison to the two deactivation zones observed over fresh Mo<sub>2</sub>C. Overall, these differences in reactivity over fresh and passivated Mo<sub>2</sub>C can be explained by the different amounts of initial oxides present on their surfaces. Specifically, the formation of toluene suggests that when the carbide passivation layer is thicker, the sites on the surface behave more like those in the bulk oxide material. Although toluene production in this study was under the detection limit due to the lower HDO reactivity

of MoO<sub>3</sub> at these conditions, alkylation activity has been reported for bulk and supported MoO<sub>3</sub> catalysts when operating at higher reactant partial pressures.

Though NAP-XPS showed that both MoO<sub>3</sub> and Mo<sub>2</sub>C had surface oxycarbide (Mo<sub>x</sub>O<sub>y</sub>C<sub>z</sub>) features, the oxycarbide observed over MoO<sub>3</sub> was significantly richer in oxygen than that on the surface of Mo<sub>2</sub>C. As shown in Fig. 1, the Mo oxidation states observed for oxycarbide present on MoO<sub>3</sub> transitions between +6 and +5 oxidation states during reaction. In contrast, the oxycarbide over Mo<sub>2</sub>C shows almost no +6 or +5 oxidation states and ca. 15% +4 oxidation state without change in the course of HDO (Fig. 2). This stark difference implies that the active sites of the two catalysts must be different. In addition to the differences in oxygen content, the electronic structure of the oxycarbide is altered by the MoO<sub>3</sub> or Mo<sub>2</sub>C underlayer, in turn affecting the HDO activity. Differences in the surface composition of the catalysts will manifest as differences in reactivity, selectivity and catalyst stability.

In order to verify these differences, HDO experiments of 4-methylanisole were performed in flow reactors over Mo<sub>2</sub>C and MoO<sub>3</sub> catalysts supported on silica (see Supplementary Methods V). Supported catalysts were used for these studies to mitigate differences in surface areas generated from formation of the oxycarbide phase. HDO performed with Mo<sub>2</sub>C/SiO<sub>2</sub> at 5 bar H<sub>2</sub> and 623 K resulted in complete conversion of 4-methylanisole with a selectivity to toluene of ca. 90%, consistent with the high benzene selectivity observed in the HDO of anisole (see Supplementary Fig. 55). Under identical reaction conditions and similar space velocities, MoO<sub>3</sub>/SiO<sub>2</sub> converted 15% of 4-methylanisole with an initial selectivity to toluene of ca. 80% that reduced to ca. 60% after 14 h, and remained constant at this value thereafter (Supplementary Fig. 56). Additionally, a combined selectivity to oxygenates, comprising mostly p-cresol, dimethylanisole and dimethylphenol at steady state of approximately 30% was observed. The presence of dimethylanisole and dimethylphenol also confirmed the presence of Brønsted acid sites capable of catalysing alkylation. In contrast, negligible transalkylation activity was observed for Mo<sub>2</sub>C, consistent with the high selectivity to C–O bond cleavage and minimal alkylation observed in previous reports.<sup>26–28</sup> Comparing MoO<sub>3</sub> with Mo<sub>2</sub>C, it is apparent that oxycarbide generated from Mo<sub>2</sub>C is more reactive and selective for HDO than the oxycarbide on MoO<sub>3</sub> under identical reaction conditions.

Mo<sub>2</sub>C also showed excellent stability as it maintained 40% of its initial activity even after 140 h time on stream (Supplementary Fig. 55). The deactivation profiles obtained across two experiments were identical with first order deactivation rate constants of 0.017 h<sup>-1</sup>. We hypothesize that the higher H<sub>2</sub> pressures employed in these experiments both reduced the formation of carbonaceous deposits and aided in the faster removal of coke already formed on the catalyst surface. To investigate this hypothesis, a series of reactions were performed over fresh Mo<sub>2</sub>C catalyst where the H<sub>2</sub> pressure was varied over 1 to 6 bar (Supplementary Fig. 57). The first order deactivation rate constants were plotted against the average methane selectivity for the respective reaction conditions (see Supplementary Fig. 58). Lower deactivation rate constant is cor-

related with higher methane selectivity, implying that larger amounts of carbonaceous deposits are removed as methane at higher H<sub>2</sub> pressures, thereby significantly increasing catalyst stability. This deactivation mode is consistent with the higher C–Mo ratios observed by NAP-XPS over the carbide material during reaction.

In summary, both MoO<sub>3</sub> and Mo<sub>2</sub>C are both promising HDO catalysts, capable of converting biomass-based oxygenate molecules to more valuable fuels and chemicals. Both catalysts were investigated for HDO of anisole at 1 mbar, 593 K while XPS spectra of Mo 3d, O 1s and C 1s were concurrently measured. MoO<sub>3</sub> and Mo<sub>2</sub>C produced benzene as the main product of HDO. Mo 3d spectra for pre-reduced MoO<sub>3</sub> show that Mo<sup>5+</sup> initially gets oxidized to Mo<sup>6+</sup>, followed by reduction to regenerate Mo<sup>5+</sup> during the course of HDO reaction. In contrast, the Mo 3d spectra of fresh Mo<sub>2</sub>C revealed that the dominant carbide phase (Mo<sup>2+</sup>) was retained throughout the HDO reaction, with no significant changes in the distribution of surface Mo species, which also included a small proportion of surface oxide species (ca. 0.20 nm overlayer). The carbide materials appeared to deactivate mainly via coking. An experiment with passivated Mo<sub>2</sub>C (Mo<sub>2</sub>C-pass) generated toluene in addition to benzene, demonstrating that the presence of oxide moieties generate acid sites sufficiently strong to promote alkylation.

Overall, our findings are largely consistent with the observations of Bhan and co-workers, wherein the dominant carbide phase is associated with a highly selective HDO product. While the surface of fresh Mo<sub>2</sub>C is predominantly carbide in nature (~85% Mo<sup>2+</sup>) throughout the reaction, it still has some oxidic character (~15% total of Mo<sup>4+</sup>, Mo<sup>5+</sup> and Mo<sup>6+</sup>). This observation suggests that high HDO selectivity over Mo<sub>2</sub>C can be attributed to some adsorbed oxygen on the Mo<sub>2</sub>C surface,<sup>26</sup> resulting in the formation of just benzene from anisole. Taken together, NAP-XPS experiments over Mo<sub>2</sub>C and passivated Mo<sub>2</sub>C reveal that surface oxygen is likely necessary for selective HDO but too much surface oxygen makes the catalyst behave more like MoO<sub>3</sub>, resulting in the production of alkylation side products. Hence, controlling surface oxygen concentration on the surface oxycarbide phase is critical for controlling HDO reactivity and product selectivity.

## Methods

**Preparation of materials.** Anisole (99 %) was used as the reactant, and purchased from VWR International. Bulk MoO<sub>3</sub> (≥99.5%) and molybdenum oxide (MoO<sub>2</sub>, ≥99 %) were purchased from Sigma-Aldrich. Bulk MoO<sub>3</sub> was pre-reduced for 3 h at 593 K, 1.013 bar under a H<sub>2</sub> flow (70 ml/min) to generate undercoordinated sites and remove the induction period reported in our previous study.<sup>15</sup> Pre-reduced MoO<sub>3</sub> was transferred to the glovebox and sealed in a vial to prevent any oxidation. Fresh Mo<sub>2</sub>C was synthesized from ammonium paramolybdate tetra (para)hydrate ((NH<sub>4</sub>)<sub>6</sub>Mo<sub>7</sub>O<sub>24</sub>·4H<sub>2</sub>O, 99%, Alfa Aesar) using a temperature programmed reaction method. Ammonium paramolybdate was loaded into a ¼ inch U-tube reactor, dispersed on top of a quartz wool plug, in contact with a K-type thermocouple (Omega, model TJ36-CAXL-u6u). The reactor was then placed in a furnace



(Carbolite, model GTF 11/50/750B), connected to a temperature controller (Digi-Sense, model 68900-10). Ammonium paramolybdate tetra (para)hydrate was heated in a 21% CH<sub>4</sub>-H<sub>2</sub> mixture (70 ml/min total flow) from room temperature to 923 K at 3 K/min and held at 923 K for 1 hour. The resulting sample (Mo<sub>2</sub>C) was then held under pure H<sub>2</sub> flow (55 ml/min) at 923 K for another hour to scavenge residual surface carbon. The sample was cooled down under H<sub>2</sub> flow to room temperature. This U-tube reactor was equipped with valves for isolation of the catalyst, to prevent any exposure to air. Once room temperature was reached, the U-tube was then transferred to a nitrogen-filled glove box and the resulting Mo<sub>2</sub>C catalyst was transferred to a 5 ml borosilicate glass ampule (Wheaton) and capped with a septum. These ampules were then evacuated on a Schlenk line outside of the glovebox, before being flame sealed. Passivated Mo<sub>2</sub>C (Mo<sub>2</sub>C-pass) was prepared under similar carburization conditions in a tube furnace, before being passivated with 1% O<sub>2</sub>-N<sub>2</sub> mixture for 2 h and then being exposed to ambient atmosphere.

**Powder X-ray Diffraction (PXRD).** PXRD was performed on a Bruker D8 diffractometer using Nickel-filtered Cu-K $\alpha$  radiation ( $\lambda = 1.5418 \text{ \AA}$ ). PXRD patterns were acquired on a 2D image plate, rotated at 15 rpm for  $2\theta$  values ranging from 20° to 90° with a step size of 0.04° and a scan speed of 0.2 s per step.

**Near Ambient Pressure X-ray Photoelectron Spectroscopy (NAP-XPS) Experiments.** NAP-XPS experiments were performed at the ISSS end-station of the Bessy II synchrotron facility in Berlin, Germany.<sup>32</sup> The set up consisted of a differentially pumped electrostatic lens system and a SPECS hemispherical electron analyser. Detailed explanation of the set up can be found elsewhere.<sup>32</sup> To ensure equal surface sensitivity, Mo 3d, O 1s and C 1s core-level regions were recorded using selected photon energies such that ejected photoelectrons had similar kinetic energy (~245 eV) across the different elements. This kinetic energy corresponds to a 0.66 nm inelastic mean free path (IMFP) for Mo<sub>2</sub>C and 0.78 nm for MoO<sub>3</sub> based on the NIST Electron IMFP Database.<sup>60</sup> Given that the information depth is roughly three times the IMFP value, ~95% of the ejected photoelectrons arise from a depth of ca. 2.0 and 2.3 nm, approximately the top 10 and 7 atomic layers of Mo<sub>2</sub>C (Mo-C bond 0.206 nm)<sup>56</sup> and MoO<sub>3</sub> (Mo-O bond 0.318 nm)<sup>56</sup> respectively. The spot size was 300  $\mu\text{m}$  x 100  $\mu\text{m}$  and the beam was moved to a new spot on the catalyst pellet (*vide infra*) for every set of XPS spectra measurement to minimize beam-induced reduction of molybdenum species.<sup>41</sup> XPS spectra were acquired in normal emission geometry with a pass energy of 20 eV and a step size of 0.05 eV for Mo 3d and 0.1 eV for C 1s and O 1s. At each time point, the elemental core level spectra were measured sequentially in this order: Mo 3d, C 1s and O 1s. For each elemental core level, typically 5-8 scans were recorded. In total, the duration of spectrum acquisition for each elemental core level was ca. 5 min. All the XPS spectra shown in the manuscript and Supplementary Information correspond to the catalyst state measured at that

time point, with the time stamp referring to the start of Mo 3d core level spectra acquisition. Binding energies for each element were corrected using their respective second-order peak. After binding energy correction, the spectra were normalized and a Shirley background was applied.<sup>61</sup> The spectra were then deconvoluted by least-square fitting of Gaussian-Lorentzian profiles using the software Plot,<sup>62</sup> with exponential tail contributions added to account for the asymmetry in some of the peaks. Density functional theory (DFT) calculations were performed for metallic Mo, MoO<sub>2</sub> and Mo<sub>2</sub>C to determine the joint density of states from which the theoretical XPS line shapes (see Supplementary Fig. 2) were generated to serve as references for the identification of the binding energies of the various constituent contributions for each compound (see Supplementary Table 1). Two sets of optimization parameters were determined based on analysing multiple spectra to best fit the MoO<sub>3</sub> and Mo<sub>2</sub>C spectra (see Supplementary Tables 2-5 and Supplementary Figs. 3, 4). Then, the same set of parameters was used consistently across the MoO<sub>3</sub> and Mo<sub>2</sub>C samples, respectively. The following constraints were used to determine the best optimization parameters: 1) spin-orbit splitting of 3.15-3.20 eV for Mo 3d<sub>5/2</sub> and 3d<sub>3/2</sub>, 2) area ratio of 3:2 for Mo 3d<sub>5/2</sub>-Mo 3d<sub>3/2</sub>, and 3) equal Gaussian-Lorentzian ratio for Mo 3d<sub>5/2</sub>-Mo 3d<sub>3/2</sub>. For quantitative elemental analysis, the raw areas for each element were integrated and then normalized by their respective photon flux and photoionization cross-sections and asymmetry parameters (see Supplementary Methods IV, Supplementary Tables 7-10 and Supplementary Fig. 5).

Pre-reduced MoO<sub>3</sub> and fresh Mo<sub>2</sub>C catalyst powders were pressed into pellets (7 mm diameter) using a hand-held pellet press (Pike Technologies) in a nitrogen-filled glovebox. Fresh MoO<sub>3</sub>, MoO<sub>2</sub> and passivated Mo<sub>2</sub>C (Mo<sub>2</sub>C-pass) were pelletized in ambient atmosphere. The catalyst pellet was then placed between two stainless steel plates, which were then mounted onto a sapphire plate, and secured with screws. Temperature was measured using a K-type thermocouple, which was wound around the screws, pressed firmly against the back plate, very close to the catalyst pellet. The air-sensitive pellets were moved from the glovebox to the NAP-XPS set up using a transfer vessel, which was then mounted directly onto the XPS set up, thereby minimizing air exposure. The sample was locally heated using laser irradiation of the unpolished back plate. All NAP-XPS experiments were typically run at 1 mbar. The gas flows and pressure of the reaction chamber were regulated using multiple mass flow controllers (MFCs, Bronkhorst) and motorized control valves. Anisole feed was introduced to the reaction chamber using a stainless steel saturator in the form of a H<sub>2</sub>-anisole saturated stream. H<sub>2</sub> gas was initially saturated with anisole in the saturator at room temperature and at 1.013 bar using a MFC set at 30 ml/min. This corresponds to a H<sub>2</sub>/anisole molar ratio of ~215. A part of this flow was delivered to the reaction chamber held at 1 mbar via a low  $\Delta P$  MFC (17-20 ml/min). The rest of the saturated gas stream was directed to the vent. All catalyst samples were heated at 5 K/min from room temperature to 593 K, and maintained at 593 K throughout the experiments. MoO<sub>3</sub> and MoO<sub>2</sub> were heated in a N<sub>2</sub> flow (10 ml/min) while Mo<sub>2</sub>C catalysts

were heated under a H<sub>2</sub> flow (10 ml/min), before switching to H<sub>2</sub>-anisole mixture (17-20 ml/min) for all reactions at 593 K. During reaction, the gas phase composition was monitored using a 4-channel micro gas chromatograph (micro-GC, CP-4900, Varian Inc), equipped with thermal conductivity detectors. The micro-GC consists of 4 columns – 2 Molsieve 5 columns (10 m and 20 m), a PoraPLOT Q column (10 m) and an Al<sub>2</sub>O<sub>3</sub>/KCl column (10 m). The PoraPLOT Q (PPQ) column was predominantly used to track benzene and anisole. All the columns were held isothermal at the following temperatures: 2 Molsieve columns at 328 K and 315 K, PPQ column at 453 K and Al<sub>2</sub>O<sub>3</sub>/KCl column at 423 K. Each micro-GC run lasted for about 7.3 min, before the next injection was made. Typically, when no reactions were run, the anisole-saturated H<sub>2</sub> stream was injected into the micro-GC via a bypass line (10 ml/min). When the reaction was started, the H<sub>2</sub>-anisole mixture was delivered to the reaction chamber, while the bypass was switched off. Similarly, at the end of each experiment, the H<sub>2</sub>-anisole mixture was turned off and bypass was resumed. The bypass served as a baseline reference for the amount of benzene observed in the absence of reaction.

**Data availability.** All data are available from the corresponding author upon reasonable request.

## References

1. Furimsky, E. Catalytic hydrodeoxygenation. *Appl. Catal., A* **199**, 147-190 (2000).
2. Huber, G.W., Iborra, S. & Corma, A. Synthesis of transportation fuels from biomass: chemistry, catalysts, and engineering. *Chem. Rev.* **106**, 4044-4098 (2006).
3. Choudhary, T. & Phillips, C. Renewable fuels via catalytic hydrodeoxygenation. *Appl. Catal., A* **397**, 1-12 (2011).
4. Bu, Q. et al. A review of catalytic hydrodeoxygenation of lignin-derived phenols from biomass pyrolysis. *Bioresour. Technol.* **124**, 470-477 (2012).
5. He, Z. & Wang, X. Hydrodeoxygenation of model compounds and catalytic systems for pyrolysis bio-oils upgrading. *Catal. Sustainable Energy* **1**, 28-52 (2012).
6. Ruddy, D.A. et al. Recent advances in heterogeneous catalysts for bio-oil upgrading via "ex situ catalytic fast pyrolysis": catalyst development through the study of model compounds. *Green Chem.* **16**, 454-490 (2014).
7. Tran, N., Uemura, Y., Chowdhury, S. & Ramli, A. A review of bio-oil upgrading by catalytic hydrodeoxygenation. *Appl. Mech. Mater.* **625**, 255-258 (2014).
8. Saidi, M. et al. Upgrading of lignin-derived bio-oils by catalytic hydrodeoxygenation. *Energy Environ. Sci.* **7**, 103-129 (2014).
9. Schutyser, W. et al. Influence of bio-based solvents on the catalytic reductive fractionation of birch wood. *Green Chem.* **17**, 5035-5045 (2015).
10. Anderson, E.M. et al. Reductive Catalytic Fractionation of Corn Stover Lignin. *ACS Sustainable Chem. Eng.* **4**, 6940-6950 (2016).
11. Anderson, E., Crisci, A., Murugappan, K. & Roman-Leshkov, Y. Bifunctional Molybdenum Polyoxometalates for the Combined Hydrodeoxygenation and Alkylation of Lignin-Derived Model Phenolics. *ChemSusChem* **10**, 2226-2234 (2017).
12. Venkatakrishnan, V.K., Delgass, W.N., Ribeiro, F.H. & Agrawal, R. Oxygen removal from intact biomass to produce liquid fuel range hydrocarbons via fast-hydrolysis and vapor-phase catalytic hydrodeoxygenation. *Green Chem.* **17**, 178-183 (2015).
13. Anderson, E.M. et al. Flowthrough Reductive Catalytic Fractionation of Biomass. *Joule* **1**, 613-622 (2017).
14. Prasomsri, T., Nimmanwudipong, T. & Román-Leshkov, Y. Effective hydrodeoxygenation of biomass-derived oxygenates into unsaturated hydrocarbons by MoO<sub>3</sub> using low H<sub>2</sub> pressures. *Energy Environ. Sci.* **6**, 1732-1738 (2013).
15. Prasomsri, T., Shetty, M., Murugappan, K. & Román-Leshkov, Y. Insights into the catalytic activity and surface modification of MoO<sub>3</sub> during the hydrodeoxygenation of lignin-derived model compounds into aromatic hydrocarbons under low hydrogen pressures. *Energy Environ. Sci.* **7**, 2660-2669 (2014).
16. Shetty, M., Murugappan, K., Prasomsri, T., Green, W.H. & Roman-Leshkov, Y. Reactivity and stability investigation of supported molybdenum oxide catalysts for the hydrodeoxygenation (HDO) of m-cresol. *J. Catal.* **331**, 86-97 (2015).
17. Murugappan, K. et al. Supported molybdenum oxides as effective catalysts for the catalytic fast pyrolysis of lignocellulosic biomass. *Green Chem.* **18**, 5548-5557 (2016).
18. Zhou, G., Jensen, P.A., Le, D.M., Knudsen, N.O. & Jensen, A.D. Atmospheric Hydrodeoxygenation of Biomass Fast Pyrolysis Vapor by MoO<sub>3</sub>. *ACS Sustainable Chem. Eng.* **4**, 5432-5440 (2016).
19. Nolte, M.W., Zhang, J. & Shanks, B.H. Ex situ hydrodeoxygenation in biomass pyrolysis using molybdenum oxide and low pressure hydrogen. *Green Chem.* **18**, 134-138 (2016).
20. Shetty, M., Murugappan, K., Green, W.H. & Román-Leshkov, Y. Structural Properties and Reactivity Trends of Molybdenum Oxide Catalysts Supported on Zirconia for the Hydrodeoxygenation of Anisole. *ACS Sustainable Chem. Eng.* **5**, 5293-5301 (2017).
21. Ren, H. et al. Selective hydrodeoxygenation of biomass-derived oxygenates to unsaturated hydrocarbons using molybdenum carbide catalysts. *ChemSusChem* **6**, 798-801 (2013).
22. Lee, W.-S., Wang, Z., Zheng, W., Vlachos, D.G. & Bhan, A. Vapor phase hydrodeoxygenation of furfural to 2-methylfuran on molybdenum carbide catalysts. *Catal. Sci. Technol.* **4**, 2340-2352 (2014).
23. Xiong, K., Lee, W.S., Bhan, A. & Chen, J.G. Molybdenum Carbide as a Highly Selective Deoxygenation Catalyst for Converting Furfural to 2-Methylfuran. *ChemSusChem* **7**, 2146-2149 (2014).
24. Xiong, K., Yu, W. & Chen, J.G. Selective deoxygenation of aldehydes and alcohols on molybdenum carbide (Mo<sub>2</sub>C) surfaces. *Appl. Surf. Sci.* **323**, 88-95 (2014).
25. McManus, J.R. & Vohs, J.M. Deoxygenation of glycolaldehyde and furfural on Mo<sub>2</sub>C/Mo(100). *Surf. Sci.* **630**, 16-21 (2014).
26. Lee, W.-S., Wang, Z., Wu, R.J. & Bhan, A. Selective vapor-phase hydrodeoxygenation of anisole to benzene on molybdenum carbide catalysts. *J. Catal.* **319**, 44-53 (2014).
27. Lee, W.-S., Kumar, A., Wang, Z. & Bhan, A. Chemical Titration and Transient Kinetic Studies of Site Requirements in Mo<sub>2</sub>C-Catalyzed Vapor Phase Anisole Hydrodeoxygenation. *ACS Catal.* **5**, 4104-4114 (2015).
28. Chen, C.-J., Lee, W.-S. & Bhan, A. Mo<sub>2</sub>C catalyzed vapor phase hydrodeoxygenation of lignin-derived phenolic compound mixtures to aromatics under ambient pressure. *Appl. Catal., A* **510**, 42-48 (2016).
29. Chen, C.-J. & Bhan, A. Mo<sub>2</sub>C Modification by CO<sub>2</sub>, H<sub>2</sub>O, and O<sub>2</sub>: Effects of Oxygen Content and Oxygen Source on Rates and Selectivity of m-Cresol Hydrodeoxygenation. *ACS Catal.* **7**, 1113-1122 (2017).
30. He, S., Boom, J., van der Gaast, R. & Seshan, K. Hydrolysis of lignocellulosic biomass over alumina supported Platinum, Mo<sub>2</sub>C and WC catalysts. *Front. Chem. Sci. Eng.* (2017).

31. Iida, T. et al. Encapsulation of molybdenum carbide nanoclusters inside zeolite micropores enables synergistic bifunctional catalysis for anisole hydrodeoxygenation. *ACS Catal.* **7**, 8147–8151 (2017).
32. Knop-Gericke, A. et al. X-Ray Photoelectron Spectroscopy for Investigation of Heterogeneous Catalytic Processes. *Adv. Catal.* **52**, 213–272 (2009).
33. Patt, J., Moon, D.J., Phillips, C. & Thompson, L. Molybdenum carbide catalysts for water–gas shift. *Catal. Lett.* **65**, 193–195 (2000).
34. Sullivan, M.M., Chen, C.-J. & Bhan, A. Catalytic deoxygenation on transition metal carbide catalysts. *Catal. Sci. Technol.* **6**, 602–616 (2016).
35. Choi, J.-S., Bugli, G. & Djéga-Mariadassou, G. Influence of the degree of carburization on the density of sites and hydrogenating activity of molybdenum carbides. *J. Catal.* **193**, 238–247 (2000).
36. Song, Z. et al. Molecular level study of the formation and the spread of MoO<sub>3</sub> on Au (111) by scanning tunneling microscopy and X-ray photoelectron spectroscopy. *J. Am. Chem. Soc.* **125**, 8059–8066 (2003).
37. Clayton, C. & Lu, Y. Electrochemical and XPS evidence of the aqueous formation of Mo<sub>2</sub>O<sub>3</sub>. *Surf. Interface Anal.* **14**, 66–70 (1989).
38. Marin-Flores, O., Scudiero, L. & Ha, S. X-ray diffraction and photoelectron spectroscopy studies of MoO<sub>2</sub> as catalyst for the partial oxidation of isooctane. *Surf. Sci.* **603**, 2327–2332 (2009).
39. Sian, T.S. & Reddy, G. Optical, structural and photoelectron spectroscopic studies on amorphous and crystalline molybdenum oxide thin films. *Sol. Energy Mater. Sol. Cells* **82**, 375–386 (2004).
40. Scanlon, D.O. et al. Theoretical and experimental study of the electronic structures of MoO<sub>3</sub> and MoO<sub>2</sub>. *J. Phys. Chem. C* **114**, 4636–4645 (2010).
41. Baltrusaitis, J. et al. Generalized molybdenum oxide surface chemical state XPS determination via informed amorphous sample model. *Appl. Surf. Sci.* **326**, 151–161 (2015).
42. Frank, B., Cotter, T.P., Schuster, M.E., Schlögl, R. & Trunschke, A. Carbon dynamics on the molybdenum carbide surface during catalytic propane dehydrogenation. *Chemistry–A European Journal* **19**, 16938–16945 (2013).
43. Oshikawa, K., Nagai, M. & Ormi, S. Characterization of molybdenum carbides for methane reforming by TPR, XRD, and XPS. *J. Phys. Chem. B* **105**, 9124–9131 (2001).
44. Ledoux, M.J., Huu, C.P., Guille, J. & Dunlop, H. Compared activities of platinum and high specific surface area Mo<sub>2</sub>C and WC catalysts for reforming reactions: I. Catalyst activation and stabilization: Reaction of n-hexane. *J. Catal.* **134**, 383–398 (1992).
45. Óvári, L., Kiss, J., Farkas, A.P. & Solymosi, F. Reactivity of Mo<sub>2</sub>C/Mo (100) toward oxygen: LEIS, AES, and XPS study. *Surf. Sci.* **566**, 1082–1086 (2004).
46. Clair, T.P.S. et al. Surface characterization of α-Mo<sub>2</sub>C (0001). *Surf. Sci.* **426**, 187–198 (1999).
47. Sugihara, M., Ozawa, K.-i., Edamoto, K. & Otani, S. Photoelectron spectroscopy study of Mo<sub>2</sub>C (0001). *Solid State Commun.* **121**, 1–5 (2001).
48. Gao, Q., Zhao, X., Xiao, Y., Zhao, D. & Cao, M. A mild route to mesoporous Mo<sub>2</sub>C–C hybrid nanospheres for high performance lithium-ion batteries. *Nanoscale* **6**, 6151–6157 (2014).
49. Delporte, P., Pham-Huu, C., Vennegues, P., Ledoux, M.J. & Guille, J. Physical characterization of molybdenum oxycarbide catalyst; TEM, XRD and XPS. *Catal. Today* **23**, 251–267 (1995).
50. Janz, G.J. Thermodynamics of the Hydrogenation of Benzene. *J. Chem. Phys.* **22**, 751–752 (1954).
51. Baddour, F.G. et al. Late-Transition-Metal-Modified β-Mo<sub>2</sub>C Catalysts for Enhanced Hydrogenation during Guaiacol Deoxygenation. *ACS Sustainable Chem. Eng.* **5**, 11433–11439 (2017).
52. Moberg, D.R., Thibodeau, T.J., Amar, F.G. & Frederick, B.G. Mechanism of hydrodeoxygenation of acrolein on a cluster model of MoO<sub>3</sub>. *J. Phys. Chem. C* **114**, 13782–13795 (2010).
53. Mei, D., Karim, A.M. & Wang, Y. Density functional theory study of acetaldehyde hydrodeoxygenation on MoO<sub>3</sub>. *J. Phys. Chem. C* **115**, 8155–8164 (2011).
54. Schaidle, J.A. et al. Experimental and computational investigation of acetic acid deoxygenation over oxophilic molybdenum carbide: surface chemistry and active site identity. *ACS Catal.* **6**, 1181–1197 (2016).
55. Liang, J. et al. Effective conversion of heteroatomic model compounds in microalgae-based bio-oils to hydrocarbons over β-Mo<sub>2</sub>C/CNTs catalyst. *J. Mol. Catal. A: Chem.* **411**, 95–102 (2016).
56. Lee, J.S., Locatelli, S., Oyama, S. & Boudart, M. Molybdenum carbide catalysts 3. Turnover rates for the hydrogenolysis of n-butane. *J. Catal.* **125**, 157–170 (1990).
57. Bej, S.K., Bennett, C.A. & Thompson, L.T. Acid and base characteristics of molybdenum carbide catalysts. *Appl. Catal., A* **250**, 197–208 (2003).
58. Sullivan, M.M., Held, J.T. & Bhan, A. Structure and site evolution of molybdenum carbide catalysts upon exposure to oxygen. *J. Catal.* **326**, 82–91 (2015).
59. Baddour, F.G., Nash, C.P., Schaidle, J.A. & Ruddy, D.A. Synthesis of α-MoC<sub>1-x</sub> Nanoparticles with a Surface-Modified SBA-15 Hard Template: Determination of Structure–Function Relationships in Acetic Acid Deoxygenation. *Angew. Chem. Int. Ed.* **55**, 9026–9029 (2016).
60. Powel, C. & Jablonski, A. NIST Electron Inelastic-Mean-Free-Path Database, Version 1.2, SRD 71. *National Institute of Standards and Technology, Gaithersburg, MD, USA* (2010).
61. Roiaz, M. et al. Reverse Water–Gas Shift or Sabatier Methanation on Ni (110)? Stable Surface Species at Near-Ambient Pressure. *J. Am. Chem. Soc.* **138**, 4146–4154 (2016).
62. Wesemann, M. & Thijsse, B.J. (*Plot version 0.997*; 2007).

## Acknowledgements

This research was funded by BP through the MIT Energy Initiative Advanced Conversion Research Program and the National Science Foundation (award number 1454299). We thank Helmholtz-Zentrum Berlin for the allocation of synchrotron radiation beamtime at beamline ISSS of BESSY II. T. E. J. acknowledges the Alexander-von-Humboldt Foundation for financial support.

## Author contributions

K.M. and Y.R. conceived the research ideas and designed the experiments. K.M. prepared the materials and performed PXRD. K.M., E.M.A., D.T. and K.S. performed the NAP-XPS experiments. K.M. and D.T. analysed the XPS data. T.E.J. performed DFT calculations. K.M. and Y.R. co-wrote the paper. Y.R. supervised the project. All authors discussed the results and commented on the different versions of the manuscript.

## Competing interests

The authors declare no competing interest.

## Additional information

Supplementary information is available for this paper at <https://doi.org/>

**Reprints and permissions information** is available at [www.nature.com/reprints](http://www.nature.com/reprints)

**Correspondence and requests for materials** should be addressed to Y.R.

**Publisher's note:** Springer Nature remains neutral with regard to jurisdictional claims in published maps and institutional affiliations.